



LAWRENCE
LIVERMORE
NATIONAL
LABORATORY

Collisionless shock experiments with lasers and observation of Weibel instabilities

H. S. Park, C. M. Huntington, F. Fiuza, R. P. Drake, D. Froula, G. Gregori, M. Koenig, N. L. Kugland, C. C. Kuranz, D. Lamb, M. C. Levy, C. K. Li, J. Meinecke, T. Morita, R. Petrasso, B. A. Remington, H. Rinderknecht, M. Roserberg, J. S. Ross, D. D. Ryutov, Y. Sakawa, A. Spitkovsky, H. Takabe, P. Tzeferacos, S. V. Weber, A. B. Zylstra

December 19, 2014

Physics of Plasmas

Disclaimer

This document was prepared as an account of work sponsored by an agency of the United States government. Neither the United States government nor Lawrence Livermore National Security, LLC, nor any of their employees makes any warranty, expressed or implied, or assumes any legal liability or responsibility for the accuracy, completeness, or usefulness of any information, apparatus, product, or process disclosed, or represents that its use would not infringe privately owned rights. Reference herein to any specific commercial product, process, or service by trade name, trademark, manufacturer, or otherwise does not necessarily constitute or imply its endorsement, recommendation, or favoring by the United States government or Lawrence Livermore National Security, LLC. The views and opinions of authors expressed herein do not necessarily state or reflect those of the United States government or Lawrence Livermore National Security, LLC, and shall not be used for advertising or product endorsement purposes.

Collisionless shock experiments with lasers and observation of Weibel instabilities^{a)}

H. -S. Park^{1,b)}, C. M. Huntington¹, F. Fiuza¹, R. P. Drake², D. H. Froula³, G. Gregori⁴, M. Koenig⁵, N. L. Kugland⁶, C. C. Kuranz², D. Lamb⁷, M. C. Levy¹, C. K. Li⁸, J. Meinecke⁴, T. Morita⁹, R. Petrasso⁸, B. A. Remington¹, H. Rinderknecht⁸, M. Rosenberg⁸, J. S. Ross¹, D. D. Ryutov¹, Y. Sakawa⁹, A. Spitkovsky¹⁰, H. Takabe⁹, P. Tzeferacos⁷, S. V. Weber¹, A. B. Zylstra^{8,1}

¹ Lawrence Livermore National Laboratory, Livermore, CA 94550, USA

² University of Michigan, Ann Arbor, MI 48109, USA

³ University of Rochester, Laboratory for Laser Energetics, Rochester, NY 14636, USA

⁴ University of Oxford, Parks Road, Oxford, OX1 3PU, UK

⁵ LULI, Ecole Polytechnique, Palaiseau, France

⁶ Lam Research Corporation, Fremont, CA 94538, USA

⁷ University of Chicago, Chicago, CA 94538, USA

⁸ Massachusetts Institute of Technology, Cambridge, MA 02139, USA

⁹ Institute of Laser Engineering, Osaka University, Osaka 565-0871, Japan

¹⁰ Princeton University, Princeton, NJ 08544, USA ^{b)}

(Dated: 13 December 2014)

Astrophysical collisionless shocks are common in the universe, occurring in supernova remnants, gamma ray bursts, and protostellar jets. They appear when the ion-ion collision mean free path is much larger than the system size. It is believed that such shocks could be mediated via the electromagnetic Weibel instability in astrophysical environments without pre-existing magnetic fields. Here we present laboratory experiments using high-power lasers and investigate the dynamics of high Mach number collisionless shock formation in two interpenetrating plasma streams. Our recent proton probe experiments on Omega show the characteristic filamentary structures of the Weibel instability, that are electromagnetic in nature with an inferred magnetization level as high as $\sim 1\%$ ¹. These results imply significant electromagnetic instabilities in the interaction of plasmas at astrophysical conditions.

PACS numbers: Valid PACS appear here

Keywords: Suggested keywords

I. INTRODUCTION

Astrophysical collisionless shocks have been of keen interests to the astrophysical community as a mechanism for self-generating magnetic fields and cosmic ray acceleration. A collisionless shock is the condition where the Coulomb mean free path is much larger than the system, yet a shock is formed via plasma instabilities. There are many astrophysical objects, both relativistic and non-relativistic, that show these characteristics collisionless shocks such as in Supernova remnants and gamma-ray bursts. It has been recently proposed²⁻⁴ that the generation of magnetic fields can occur in these shocks on a cosmologically-fast timescale, via the Weibel instability⁵. Three-dimensional (3D) particle-in-cell (PIC) numerical simulations have confirmed that the strength and scale of Weibel-generated magnetic fields are consistent with what would be required to play a dominant role in the magnetization of astrophysical collisionless shocks [Sakai 2004]⁶⁻¹⁰. The Weibel instabilities can convert the kinetic energy to magnetic energy that can be the mech-

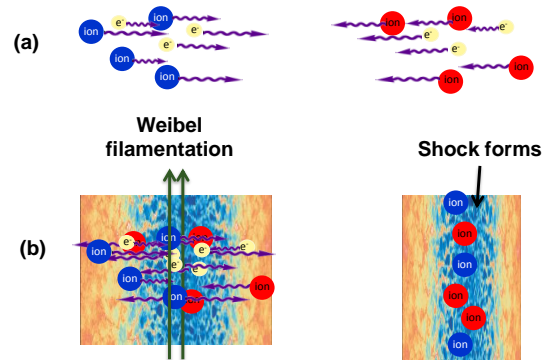


FIG. 1. Conceptual sketch of collisionless shock forming process. The high velocity plasma flows have large Coulomb mean free path where clean penetration is expected. The Weibel instability can create local magnetic field that traps the ions via $q \times \mathbf{B}$ Lorenz force and creates a shock.

anism for seed magnetic fields in universe⁵ and promote collisionless shock formation without preexisting magnetic fields.

Figure 1 shows the concept how the Weibel mediated shock could be formed where the Weibel instabilities are created from the momentum anisotropy distribution

^{a)}Paper BI2.2, Bull. Am. Phys. Soc. **59**, 4 (2014).

^{b)}Invited speaker; Electronic mail: park1@llnl.gov

of the plasma flows⁵ and create localized self-generated magnetic fields. The self-generated magnetic fields trap the ions via the Lorenz force, thereby imitating collisions in the usual collisional shocks and leading to collisionless shock formation. The signature of the instability is a pattern of current filaments stretched along the axis of symmetry of the flows. The exact understanding of the required physical condition for such occurrence has not been well characterized, and laboratory laser experiments can provide a unique platform to study the electromagnetic Weibel instabilities that occur from high-Mach number plasma flows. There are many attempts to create collisionless shocks in the laboratory; but most of them were electrostatic shocks. Only very recently, very high intensity lasers such as Omega and NIF are capable to create the condition required for creation of electromagnetic Weibel instabilities^{1,11}.

The condition required to create the collisionless shocks are: 1) the collision mean-free path λ_{mfp} for the more massive ion component (carbon, in the case of CH plasmas) should be much larger than the system size (that is, the spatial scale of the interacting flows, l_{int}): $\lambda_{mfp} \gg l_{int}$; 2) the system size, l_{int} , must be much larger than the instability scale length, l^* : $l_{int} \gg l^*$ ¹²⁻¹⁴. So, we are looking for the conditions where:

$$l^* \ll l_{int} \ll \lambda_{mfp} \quad (1)$$

Assuming that the temperature of the colliding flows is much smaller than the ion energy due to the bulk flow velocity, λ_{mfp} can be calculated by¹⁵

$$\lambda_{mfp} [cm] \sim 5 \times 10^{-13} \frac{A_Z^2 (v [cm/s])^4}{Z^4 n_z [cm^{-3}]}, \quad (2)$$

where A_Z , Z , and n_Z are the atomic weight, charge, and number density of the main ion component, and v is the flow bulk velocity before the collision with the other flow.

When evaluating the plasma instability scale length, l^* , we separate them into two types: electrostatic instabilities and electromagnetic instabilities. Electrostatic plasma instabilities, l_{ES}^* , is estimated by a model that is based on the growth-rate assessments in Ref.¹⁶:

$$l_{ES}^* \sim K \frac{v}{\omega_{pi}} \frac{W}{T_e} \quad (3)$$

where $K \gg 1$ is a numerical factor accounting for the number of the growth times required for the instability to reach a developed stage, W is the kinetic energy of the main ion component in the flow, T_e is the electron temperature (in energy units) in the flow prior to the collision, v is the bulk flow velocity, and ω_{pi} is the ion plasma frequency. Note that v/ω_{pi} is roughly the distance travelled by the flow in one ion plasma wave oscillation period. Hence, $K \gg 1$ implies that the plasma in the interaction region should correspond to many ($\gg 1$)

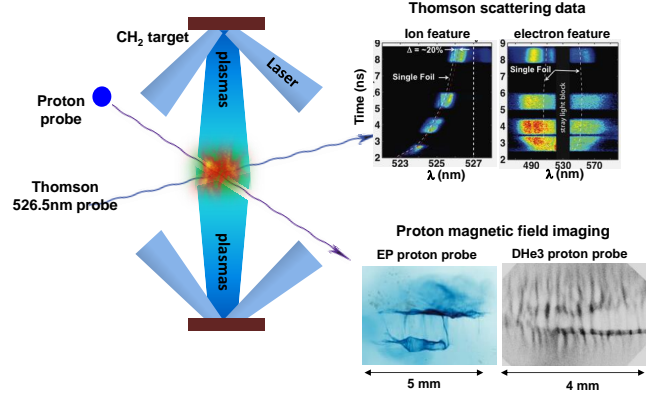


FIG. 2. Schematic of Omega experiment. We use Thomson scattering to probe the plasma state and proton probe to image the magnetic field structures.

plasma waves. Applying:

$$W[eV] = 5.2 \times 10^{-13} A_z (v [cm/s])^2 \quad (4)$$

Then l_{ES}^* is evaluated by:

$$l_{ES}^* [cm] \sim 10^{-3} K \frac{v [cm/s] \sqrt{A_Z} W [eV]}{Z \sqrt{n_Z [cm^{-3}]} T_e [eV]} \quad (5)$$

For the electromagnetic instability, l_{EM}^* , of the Weibel type can be evaluated by:

$$l_{EM}^* [cm] \sim 10^{-3} K' \frac{c}{\omega_{pi}}; \text{ where } K' > 1 \quad (6)$$

Here, c/ω_{pi} corresponds to ion plasma skin depth, namely, the distance light could travel in one ion plasma wave oscillation period. The factor K' indicates the level of required ion skin depth to fully form a shock. Particle-in-cell (PIC) simulations indicates that K' should be of the order of 300¹⁷. In the counter-streaming plasma experiments, the electrostatic instability will probably be dominant at the initial stage of interaction. In comparison of equations (5) and (6) to equation (2), the optimum conditions for the study of collisionless shocks favor higher flow energies and electron temperatures, and lower flow densities. Lower- Z materials are somewhat preferable as λ_{mfp} very rapidly increases for lower Z .

II. EXPERIMENTAL SETUP

Figure 2 shows our typical laser experimental configuration at the Omega laser facility¹⁸. Two face-on polyethylene (CH₂) plastic foils are illuminated by ~ 4 kJ of 351 nm laser energy with focal spot diameters of 250 μm on the target surface, generating high-velocity counter-streaming plasma flows. The separation is 8 mm between the targets.

In order to verify that we meet the condition of collisionless regime imposed in equation 1, we extensively

studied the plasma state of the single and double flows using Thomson scattering (TS)^{13?}. Thomson scattering is used to measure the plasma bulk velocity (v), electron temperature (T_e), ion temperature (T_i), and electron density (n_e). For our experiments, the probe laser of 526.5 nm studies a plasma volume of $100\ \mu\text{m} \times 100\ \mu\text{m} \times 60\ \mu\text{m}$ at the central region of the counter-streaming plasmas. Thomson scattered light is measured for two spectral ranges, a large spectral range to measure the electron feature (collective scattering from electron-plasma waves) and a narrow spectral range to measure the ion feature (collective scattering from ion-acoustic waves). An example of time composite electron and ion features from the double foil counter-streaming data is shown in the top right panel in Fig 2.

Extensive Thomson scattering data were collected for both single-flow and counter-streaming flows. Time-slices of the data from the electron feature are then fitted with the Thomson scattering form-factor allowing a measurement of the electron temperature (T_e) and electron density (n_e). With constraints from the electron feature fitting, the ion feature can then be used to measure the ion temperature (T_i) and bulk plasma flow velocity (v). This can be understood from the simplified dispersion relation, $\Delta\lambda = \frac{4\lambda_{probe}}{c}\sin(\theta/2)\sqrt{\frac{ZT_e}{M} + \frac{3T_i}{M}}$. The details of these measurements can be found in Refs^{13,19}.

Our detailed measurements indicate that the bulk flow velocity is $> 1000\ \text{km/s}$ up to 5 ns and is not suppressed for the double flow case, indicating interpenetrating flows as seen in Figure 3 (a). The single flow n_e is $\sim 5 \times 10^{18}\ \text{cm}^{-3}$ at maximum and is doubled for the counter-streaming case at $1 \times 10^{19}\ \text{cm}^{-3}$ (Figure 3 (b)). This indicates that a shock is not quite formed as we should expect a factor of > 2 increase in electron and ion densities at a shock front. Another significant finding from the TS measurement is the significant increase in T_e (Figure 3 (c)) and T_i (Figure 3 (d)) for the counter-streaming double flows. The T_e was $\sim 200\ \text{eV}$ for the single flow whereas the double flow T_e was up to 1 keV increase. The rapid T_e increase at early time is explained by electron-ion collisions from ion slowing-down by drag forces caused by the ‘resting’ electron gas¹². While this drag-force model explained the T_e increase very well, the ion-ion collisions could not explain the observed T_i increase. When collisional particle-in-cell (PIC) simulations are applied accounting for acoustic two-stream electrostatic instabilities, we are able to reproduce the T_i increase. This instability occurs for $T_e > T_i$ and therefore leads to the heating of the ions to temperatures close to T_e . Our quantitative plasma state measurements suggest that the intra-flow ion and electron collisional effects are important and that inter-flow ion collisions are rare from high velocity flows.

Using the measured plasma parameters, l_{EM}^* , l_{ES}^* , l_{int} , and λ_{mfp} are calculated using the equations above. As shown in Figure 4, λ_{mfp} is much larger than the instability unit scale lengths demonstrating we are in col-

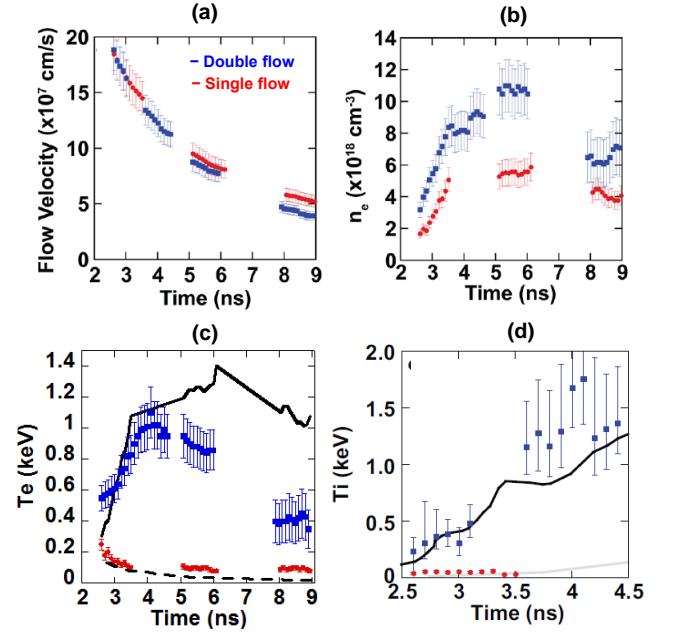


FIG. 3. Plasma parameters measured by the Thomson scattering of single and double flows: a) flow velocity; b) electron density; c) electron temperature; d) ion temperature.^{13,19}

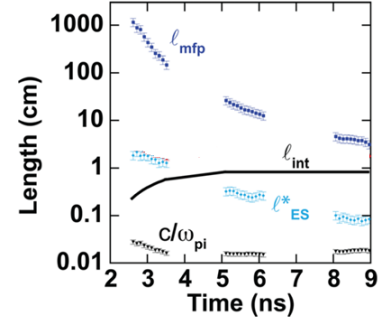


FIG. 4. Coulomb mean free paths and instability scale lengths by the equations (5) and (6)¹³.

lisionless regime.

In our experiments, the magnetic field structure of the forming collisionless shock is characterized using proton probes. We use two different proton sources: 1) short pulse generated protons by the target-normal sheath acceleration mechanism²⁰; and 2) imploding a capsule filled with deuterium (D) and helium-3 (^3He) fuel. The short pulse generated protons are generated by illuminating a 10 ps pulse of up to 800 J of 1053 nm infrared light onto $40\ \mu\text{m}$ diameter spot for an intensity of $\sim 2 \times 10^{18}\ \text{W/cm}^2$ on an Au disk target. Electric and magnetic fields deflect the protons which are then recorded on radiochromic film layered with Al filters to obtain a range of proton energies from 5 to 15 MeV.

We also use the 14.7 MeV and 3 MeV mono-energetic proton source generated by thermonuclear interactions of $\text{D} + ^3\text{He} \rightarrow ^4\text{He} + \text{p}$ (14.7 MeV) and $\text{D} + \text{D} \rightarrow \text{t} + \text{p}$ (3

MeV)²¹. For our experiments, the 2 μm thin silica capsules are filled with 18 atm D^3He fuel (6 atm of D and 12 atm of ^3He for equal atomic distribution) and are compressed uniformly by ~ 9 kJ of laser energy from 18 laser beams. The protons are generated at the peak of compression creating $\sim 10^8$ protons isotropically lasting ~ 50 ps with a source size of ~ 50 μm in diameter. A 10x10cm CR-39 detector pack was placed 27cm from the object plane for a magnification $M=27$ and a 3.7mm field of view. The pack consists of two layered and filtered pieces of 1.5mm thick CR-39; the first piece detects the DD-p and has a 12.5 μm thick Ta filter while the second piece has an additional 150-200 μm Al filter and detects the D^3He -p. The filtering serves to eliminate laser-generated fast ions and to range the protons to an optimal energy for CR-39 detector²². Each piece of CR-39 is etched in a NaOH solution to reveal the proton tracks and then scanned on a microscope system, which records the location and characteristics of each particle track. In the analysis, limits on the contrast, eccentricity, and diameter of tracks are chosen to reject background. The images displayed are a fluence histogram of the resulting signal counts with a bin size of 333 μm at the detector plane, which was chosen for high resolution with adequate statistics per bin. Examples of these two proton magnetic field imaging are shown in the right-bottom panel in Figure 2.

III. OBSERVATION OF SELF-ORGANIZING FIELDS USING SHORT PULSE GENERATED PROTON SOURCE

Using proton probes generated by short pulse lasers on EP, we observe large, stable, reproducible electromagnetic field structures that arise in counter-streaming interpenetrating supersonic plasma flows in the laboratory. Self-organization, whereby energy progressively transfers from smaller to larger scales in an inverse cascade, is widely observed in fluid flows, such as in the nonlinear evolution of multimode Rayleigh-Taylor and Kelvin-Helmholtz instabilities. These surprising structures, predominantly oriented transverse to the primary flow direction, extend for much larger distances than the intrinsic plasma spatial scales, and persist for much longer than the plasma kinetic timescale of 10. One such example image is shown in Figure . This image is taken at 5.2 ns after the laser, and the sharp co-planar field structures are clearly visible.

Their origin is now explained by the magnetic field advection process. Here the Biermann battery magnetic field is generated near the target surface in a toroidal shape, and advects along the electron plasma flows, then recompresses near the midplane [3]. The magnetic field strength is evaluated by the caustic analysis²³ by:

$$B_{cf} = \frac{m_p c}{el} \sqrt{\frac{2W}{m_p}} \frac{d^3}{\sqrt{\pi} a^2 \sin \psi}, \quad (7)$$

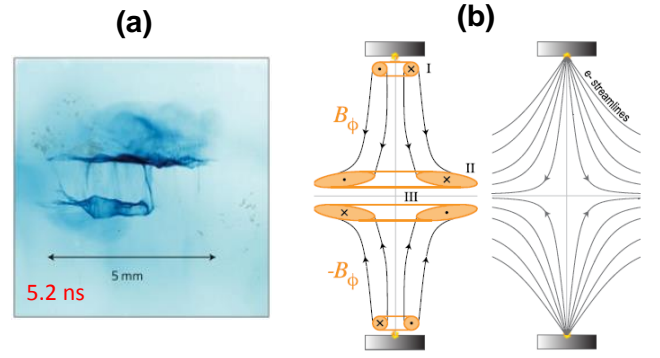


FIG. 5. (a) Omega EP short pulse generated proton image of counter-streaming plasmas at 5.2 ns after the laser. Highly stable self-organizing planar magnetic field structures are observed; (b) This is from the Biermann battery magnetic field that is generated near the target surface; advects along the electron flows; then recompress in the mid-plane [Ref].

where W is the proton kinetic energy (8.8 MeV), b/a the aspect ratio (1/20), ψ is the distance from proton source to object plane (8 mm), ψ is the tilt angle of the plane (5 to 10 degrees). When we apply our experimental measurements and observables, we derive $B_0 = 10T$. While this kind of self-organizing structures may play an important role in astrophysical conditions, we find that the magnetic field generation from this Biermann battery source is small compared to the Weibel source.

IV. OBSERVATION OF WEIBEL FILAMENTATION USING D^3He CAPSULE GENERATED PROTON SOURCE

Electromagnetic fields of the counter-streaming flows are imaged with protons generated by a D^3He imploding capsule. The advantage of the D^3He capsule generated protons are their mono-energetic properties at 14.7 MeV and 3 MeV sources and the high flux. Figure 6 shows the comparison of proton radiography image between the single flow and the counter-streaming double flows. The targets were diagonal in these images as depicted in the Figure. Strong striations in the counter-streaming double flow images are obvious along with the co-planar structures indicating that plasma instabilities created strong electromagnetic features. The filaments are likely from the Weibel induced fields whereas the co-planar features are the Biermann field recompression described in the previous section.

Figure 7 shows the compilation of the filament evolution taken over several shots including repeats. We observe a gradual increase in the spatial scale, in qualitative agreement with the growth-rate dependence on the wavelength (the shortest develop first).

To quantify the change in observed filament spacing, rectangular sections of the images are integrated to create radial intensity profiles. To highlight the regions of

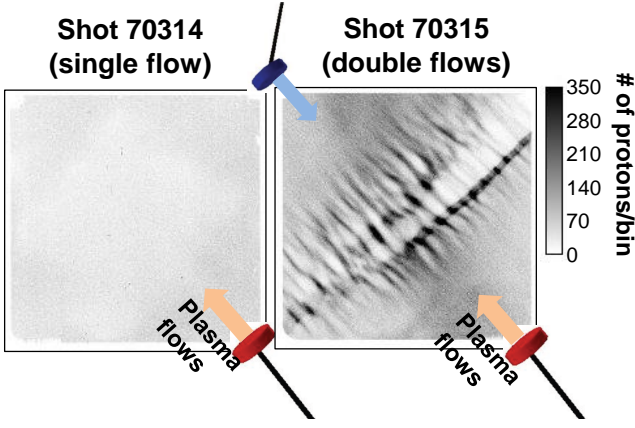


FIG. 6. D^3He proton backlighter (14.7 MeV) radiographed the electromagnetic field structures in the middle of the counter streaming plasma flows. Strong striation features are observed.

the images where there is an absence of protons, the intensity I is modified as: $f(I) = \langle I \rangle - I$, where $\langle I \rangle$ is the mean pixel value over the entire region of interest. Peaks in this profile are identified, and their relative spacing in the target plane is recorded (Fig 8 (a)). This method is applied at several locations in the image, and the measured spacing between filaments is binned for all regions.

The distribution of filament spacing is fit by a function of the form:

$$f(x|k, \mu, \sigma) = \left(\frac{1}{\sigma}\right) \exp\left(-\left(1 + k \frac{(x - \mu)}{\sigma}\right)^{-\frac{1}{k}}\right) \times \left(1 + k \frac{(x - \mu)}{\sigma}\right)^{-1 - \frac{1}{k}} \quad (8)$$

where shape, scale, and location parameters k , σ , and μ are fit according to the data²⁴. This distribution captures the observed filament spacing, which generally skew positive. In Figure 8 (b), the measured filament spacing is shown, and quantified by μ in Eqn. 8. Note that in each case, the location parameter μ matches the median observation, where the bins are incremented by the CR39 pixel size in the target plane, approximately 11 μm .

The error bars in Figure 8 (c) represent the full width at half-maximum of the fitted distribution at each time. Between 5.6 and 6.6 ns the median filament spacing is seen to be constant, but the wide error bars on the later measurements do not preclude a continued increase in filament size. The larger error bars on latest time measurement is a product of the large central region where very few protons were detected as shown the shot number 74471 in Figure 7.

V. COMPARISON WITH PIC SIMULATION

In order to understand both the Weibel and Biermann battery generated magnetic fields in our proton imaging experimental system, we have conducted detailed 3-dimensional particle-in-cell (3D PIC) simulations with OSIRIS²⁵ along with proton ray tracing through the electromagnetic field. The OSIRIS PIC simulations include with the fully electromagnetic, fully relativistic, and massively parallel processing that solves Maxwell's equations directly, resolving all the relevant physics at the electron and ion skin depth scales. The relativistic Lorentz force is used to calculate the motion of the plasma particles, and relativistic expressions are used to derive the charge and current densities from the positions and momenta of the particles. Using the measured plasma input from our experiments as described in section 2: $n_e = 5 \times 10^{18} \text{ cm}^{-3}$, $v_e = v_i = 1900 \text{ km/s}$, $T_e = T_i = 100 \text{ eV}$, comprehensive simulations are completed to show the magnetic field generation as shown in Figure 8 (a). The color scale indicates that the magnetic fields were up to $\sim 0.4 \text{ MG}$.

The simulated proton radiographs were obtained by launching a 14.7 MeV proton beam transversely to the ow propagation direction as schematically shown in Figure 9 (b). The proton distribution was initialized in OSIRIS following the distribution of an isotropic point source located 1 cm away from the beginning of the simulation box, in order to be consistent with our experimental setup. The protons probe the self-consistent fields produced in the 3D simulation and exit on the opposite side of the simulation box, being then propagated ballistically to a square detector of 13 cm \times 13 cm placed 30 cm away from the original point source, matching the experimental magnification of 30 \times . The detector has 512 \times 512 points, and ~ 10 million probing protons are collected in each image.

In addition to the filamentary Weibel structure, we also added the Biermann battery field that was described in section 4. The final proton radiography simulation results are compared with data in Figure 10 showing remarkable resemblance to the data. From the detailed studies of simulation and data, we derive the magnetization, which is defined: $\sigma = \frac{B^2/4\pi}{(\gamma-1)nmc^2}$. This is the quantity that the kinetic energy converts to magnetic energy in the system. Figure 11 shows this magnetization as a function of time. The dotted line is the field strength without pre-existing magnetic field where as the solid line is accounting for the initial field by the Biermann battery. The straight linear line is the theoretical growth rate of the ion Weibel instability. Note that the final total magnetization is 0.01 and the initial Biermann battery field plays little role in the magnetization growth. The Weibel instability filamentation is clearly observed in the laboratory and a significant self-generated magnetization is indicated¹.

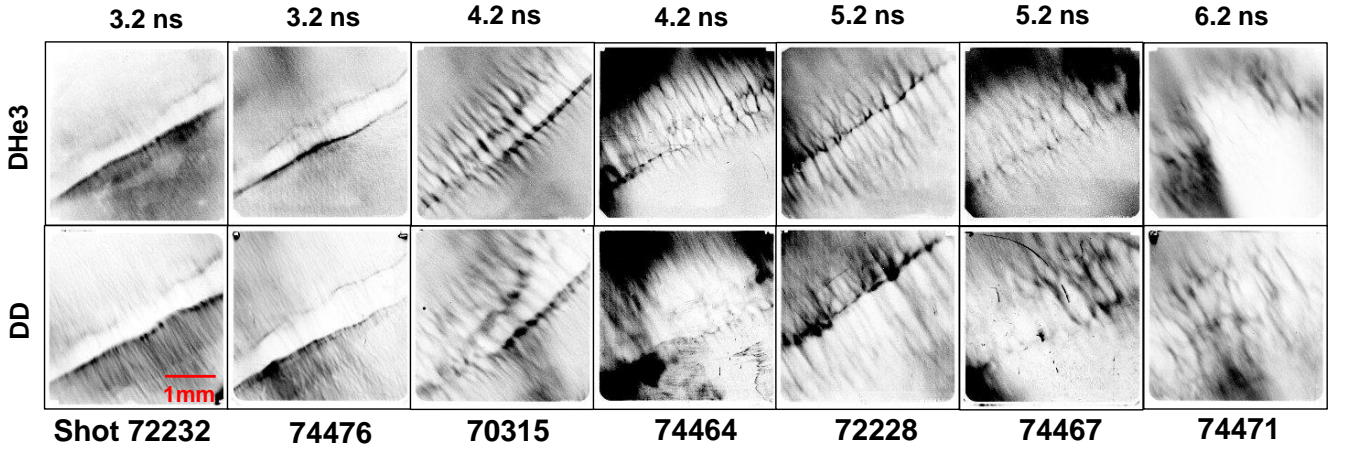


FIG. 7. Compilation of proton radiography images taken over several shots and different timings. We have repeated a set to see the repeatability of filament evolution.

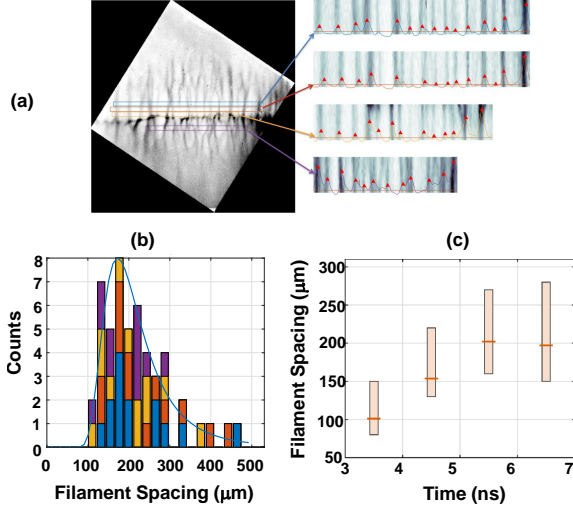


FIG. 8. Calculation of filament spacing in D^3He images. a) Regions of the CR39 image are selected for analysis. For the 5.6 ns image shown here, regions of interest are shown in different colors. b) For each region, the mean pixel intensity is calculated per column. The resulting profile is subtracted from the mean pixel value, to produce a 1D profile where the absence of protons (dark regions in the image) correspond to peaks in the profile (colored profiles). Peaks in the profile are identified (red triangles) and the spacing between the peaks is recorded. b) A histogram of the spacing of the filaments is generated, and the distribution is fit according to equation 8. The same analysis is performed for each CR39 image. c) Filament spacing as a function of time.

VI. WEIBEL THEORY AND DISCUSSION

The Weibel instability was first considered for electron plasmas with anisotropic electron distributions⁵ and resulted in a purely electron mode, with the ions forming a uniform background. This mode has a peculiar feature; its growth rate is anisotropic, strongly favoring modes

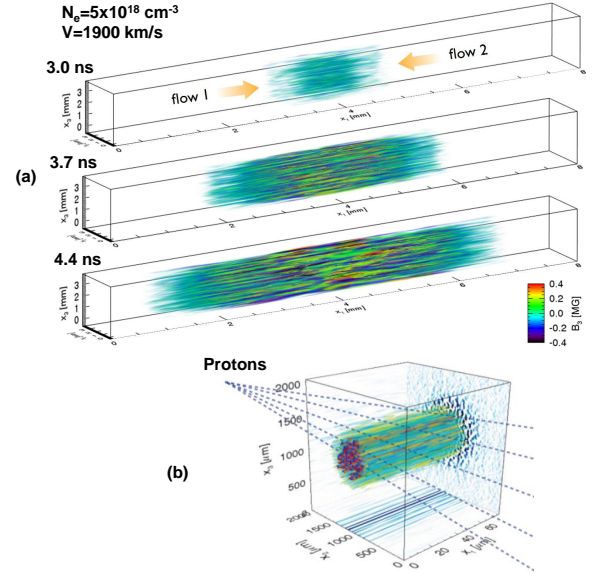


FIG. 9. (a) 3D OSIRIS PIC simulation of interpenetrating flows and the magnetic field generation via Weibel instability; (b) Illustrative geometry of the proton radiography in 3D PIC simulations used to make comparison with the experimental data. The protons probe the self-consistent fields produced in the 3D interaction of the flows and are then projected to the detector.

with wave-vectors perpendicular to the electron distribution's symmetry axis. As directions (x, y) in the plane perpendicular to the axis of symmetry (z) are equivalent, the modes acquire a characteristic filamentary structure, with the filaments parallel to z . The modes are electromagnetic, with significant perturbation of the magnetic field.

Later similar electromagnetic modes have been analyzed in other settings, including modes driven by relativistic counter-streaming electron and positron

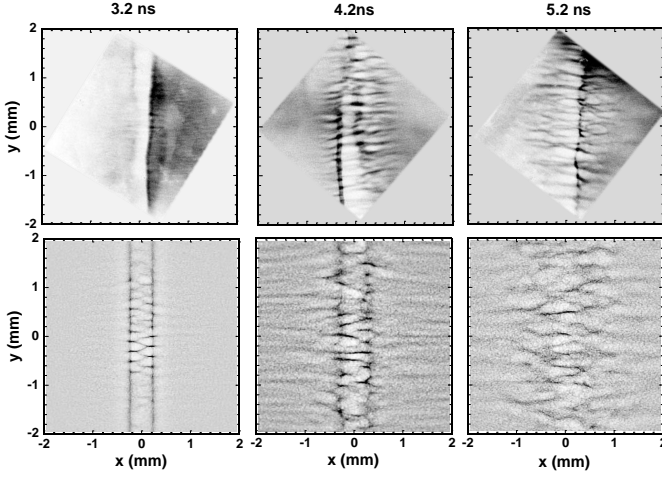


FIG. 10. Comparison between the simulated proton radiography of 3D PIC magnetic fields and the experimental data. Their resemblance are remarkable indicating that the magnetization from the interpenetrating flow was high.

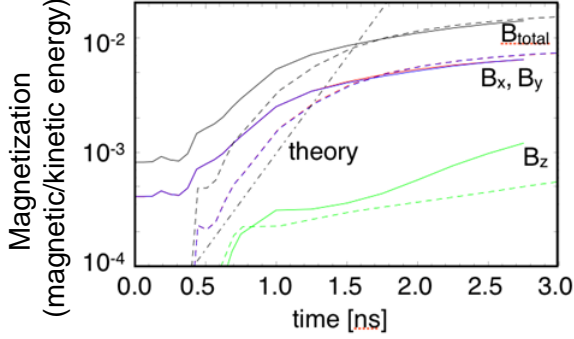


FIG. 11. Magnetization inferred from the PIC simulation. The data indicates that we achieved upto 1% magnetization.

plasmas^{7,26} and modes driven by counter-streaming ion flows¹⁷. It is the latter, ion-driven version that is thought to be responsible for collisional shock generation and that is the focus of the present study.

The linear theory of the Weibel instability driven by collisionless counter-streaming plasmas is well developed and summarized in Ref.²⁷. For experiments of the type performed in our study we need to consider a collisional version of the Weibel instability, where the inter-stream ion collisions are negligibly rare, but intra-stream collisions are important. Especially significant can be collisions in the electron background that may cause a decrease in the growth rates. These collisional effects have been described in Ref.²⁸. To make such collisional effects insignificant, one has to take special care to work in a regime of a high electron temperature, and this condition was satisfied in our experiments. This is an important point, as a low collisionality is typical of the astrophysical environment which we are imitating.

In our experiment there exist a regular magnetic field

generated by the Biermann battery effect²⁹. This was found experimentally³⁰ by the proton deflectometry technique and explained theoretically as being generated at the targets by the Biermann battery effect³¹. The magnitude of this field is in the range of a few Tesla^{31,32}. The field is azimuthal (the field lines encircle the axis) and has opposite polarities at the opposite sides of the midplane. The “thickness” of the zone of enhanced field is about 0.5 mm on each side of the midplane; between these two zones a field reversal occurs in a region about 0.5 mm thick.

The gyroradius of 1000 km/s carbon ions in the 4 Tesla field is $\rho_i \sim 5$ mm, i.e., significantly larger than the thickness of the enhanced field zones. As the “kicks” that the ions experience when passing these two zones have opposite directions, the net effect is very minimal—essentially zero near the axis. The situation is quite different for the electrons: the gyroradius of 1 keV electrons in the 4 T field is $\rho_e \sim 25 \mu\text{m}$. This may have an effect on the electron stabilizing terms in the dispersion relation for the Weibel instability, for the modes with $k\rho_e < 1$, i.e., for the wavelengths $\lambda > 2\pi\rho_e \approx 50 \mu\text{m}$. As the observed wavelengths are typically shorter than that, the effect of the regular magnetic field is minimal.

The observed filamentary structures are localized near the midplane, extending somewhat beyond the Biermann battery “pancakes.” Their radial extent near the equatorial plane is larger than $r \sim 1$ mm. The localization near the midplane could be explained by two factors: lower growth rates at larger radii and by the advection of perturbations. To evaluate the role of these two factors, we have performed a linear stability analysis accounting for the varying density of each stream and varying flow velocity. As the experimentally observed wavelengths of perturbations are small compared to the global scale of the experiment, an eikonal approach is sufficient.

We denote the ion densities and velocities of each stream as $n_{1,2}$ and $v_{1,2}$. Switching to the frame moving with the average velocity

$$\mathbf{u} = \frac{n_1 \mathbf{v}_1 + n_2 \mathbf{v}_2}{n_1 + n_2}, \quad (9)$$

we find that in the frame moving with velocity \mathbf{u} the streams are counter-propagating, with velocities

$$\mathbf{v}'_{1,2} = \mathbf{v}_{1,2} - \mathbf{u} \pm (\mathbf{v}_1 - \mathbf{v}_2) \frac{n_{1,2}}{n_1 + n_2} \quad (10)$$

In this frame a canonical derivation of the Weibel dispersion relation for the modes propagating in the perpendicular direction to the flows yields the following dispersion relation for the growth-rate Γ :

$$\Gamma^2 = \frac{k^2 w^2}{1 + k^2 c^2 / \omega_{pi}^2}; \text{ where} \quad (11)$$

$$w^2 = \frac{n_1 n_2}{(n_1 + n_2)^2} (\mathbf{v}_1 - \mathbf{v}_2)^2 \quad (12)$$

with being an ion plasma frequency corresponding to the total ion density,

$$\omega_{pi}^2 = \frac{4\pi Z^2(n_1 + n_2)e^2}{Am_p} \quad (13)$$

Eq. (3) we have neglected a stabilizing electron term that is insignificant for the sufficiently hot electrons and is further reduced by the presence of the regular magnetic field. The growth rate Γ grows with the wave number and reaches saturation at

$$k \sim k_0 \equiv \frac{\omega_{pi}}{c} \quad (14)$$

It is usually assumed that this is a representative wave number for the filaments, determining their transverse size. The saturation level of the growth-rate (denoted as Γ_{\max}) is:

$$\Gamma_{\max} = \omega_{pi} \frac{w}{c} \quad (15)$$

In order for the instability to develop from the initial noise to the level where the Weibel filaments would become visible by our diagnostic tools, the growth rate 15 should be significantly higher than the inverse duration of the interaction, as well as the inverse time of the plasma advection from the high growth-rate zone and the shearing time (see below). To find out how the growth-rate 15 varies over the interaction domain between the two foils, we choose a model of two identical streams originating at the opposite targets separated by a distance $2L$ (so that L is the distance from the center of the interaction region to each of the targets), see Figure 12. As the laser spots on the targets are small compared to L , we assume that we have point sources, so that velocity of each stream at some point is directed along the line connecting the observation point to the point source of this stream. The sources of the streams are assumed to be identical; the density in each stream is inversely proportional to the square of the distance from the corresponding source.

For this model the maximum growth rate (Eqn. 15) is in the center. Figure 13 shows the spatial dependence of the growth rate that is near maximum over a very large region (see e.g. a 0.8 contour). This is not what is observed experimentally. So, we consider below limiting factors associated with advection and flow shearing that could limit the growth.

Figure 5 (b) shows the streamlines of the advection flow. The flow moves the perturbations in the general direction towards the midplane. This may explain the absence of the mode, say, halfway between the target and the midplane, despite essentially the same growth-rate. The advection velocity is zero near the center and grows along the radial coordinate. At larger radial distances it would advect perturbations away from the zone of the high growth-rate. This may set the limit to the radial extent of the zone with large perturbations.

The flow shear across the streamlines can also limit the width of the perturbation zone near the midplane. The

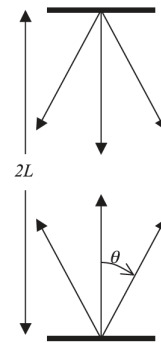


FIG. 12. The geometry of the model. The velocity of the stream at each point is parallel to the line connecting this point with the point source; the density scales inversely proportional to the square of the distance to the source (a steady flow with a constant velocity).

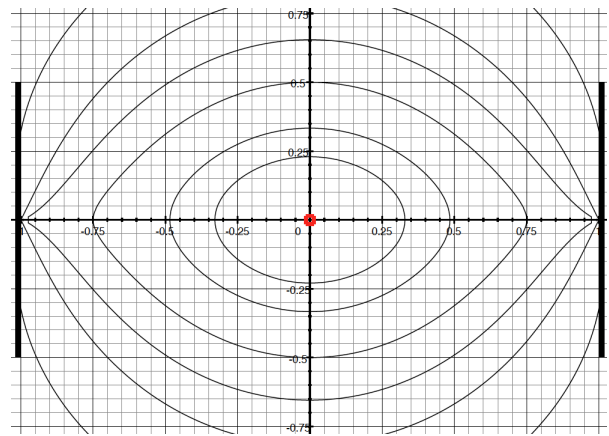


FIG. 13. The spatial dependence of the growth rate 15 normalized to its maximum situated at the center (red dot). The contours (starting from inside) correspond to the growth rates 0.95, 0.9, 0.8, 0.7, 0.6 and 0.5.

condition of a strong shearing stabilization near the mid-plane can be written as approximately $\Gamma_{\max} = |du_z/dz|$, with the derivative taken at the distance approximately equal to the thickness of the perturbed zone.

After considering all these factors, the characteristic dispersion curves for the experimental results are plotted in Fig 14.

VII. CONCLUSION

In conclusion, laser generated counter-streaming plasma flows have been studied in connection to astrophysical collisionless shocks. We observe that the intra-collisional electron-ion interaction by electron-drag force elevates the electron temperature and electrostatic instabilities raise the ion temperatures for the double flows. We detect very stable self-organizing field structures that

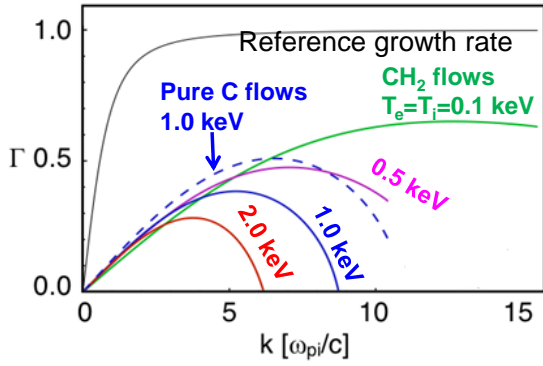


FIG. 14. Weibel growth rate vs the wave number at different electron and ion temperatures of 0.1 keV (green), 0.5 keV (magenta), 1 keV (blue and 2 keV (red))⁷.

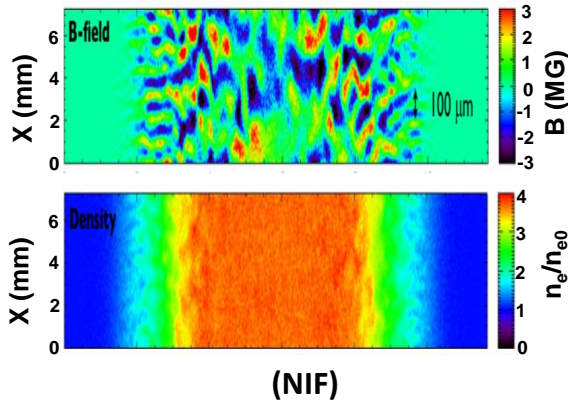


FIG. 15. 3D PIC simulation results of B-field (top) and electron density (bottom) for the NIF experiments. The NIF experiments will be able to produce fully formed collisionless shocks ($n_e/n_{e0} \sim 4$) and B field near 3 MG.

originate from the recompression of the advected Biermann battery magnetic field. The Weibel filamentation is directly imaged and a magnetization level of 1% is derived.

While these results are very unique, the Omega experiments didn't reach the instability scale length that is required to generate a fully formed shock. The NIF experiment will be able to create true Weibel mediated collisionless shocks, as indicated in Figure 15 by the PIC simulation where the density will be four folds of the initial density and the magnetic field will be up to 3 MG. Observation of this high level of magnetization will provide direct connection of astrophysical magnetic field generation and shock formation mechanism.

ACKNOWLEDGMENTS

This work was performed under the auspices of the U.S. Department of Energy by Lawrence Livermore Na-

tional Laboratory under Contract DE-AC52-07NA27344.

- ¹C. M. Huntington *et al.*, "Observation of magnetic field generation via the weibel instability in interpenetrating plasma flows," (2014), Nature Physics (accepted).
- ²R. Schlickeiser and P. K. Shukla, "Cosmological Magnetic Field Generation by the Weibel Instability," The Astrophysical Journal **599**, L57–L60 (2003).
- ³P. Chang, A. Spitkovsky, and J. Arons, "LONG-TERM EVOLUTION OF MAGNETIC TURBULENCE IN RELATIVISTIC COLLISIONLESS SHOCKS.," Astrophysical Journal **674**, 378–387 (2008), arXiv:0801.4583.
- ⁴A. Bret, "Weibel, two-stream, filamentation, oblique, bell, buneman...which one grows faster?" The Astrophysical Journal **699**, 990 (2009).
- ⁵E. S. Weibel, "Spontaneously growing transverse waves in a plasma due to an anisotropic velocity distribution," Physical Review Letters **2**, 83–84 (1959).
- ⁶M. V. Medvedev and O. V. Zakutnyaya, "Magnetic fields and cosmic rays in grbs: A self-similar collisionless foreshock," The Astrophysical Journal **696**, 2269 (2009).
- ⁷A. Spitkovsky, "On the structure of relativistic collisionless shocks in electron-ion plasmas," The Astrophysical Journal Letters **673**, L39–L42 (2008).
- ⁸M. V. Medvedev, L. O. Silva, M. Fiore, R. A. Fonseca, and W. B. Mori, "Generation of magnetic fields in cosmological shocks," Journal of the Korean astronomical society **37**, 533–541 (2004).
- ⁹T. N. Kato and H. Takabe, "Electrostatic and electromagnetic instabilities associated with electrostatic shocks: Two-dimensional particle-in-cell simulation," Physics of Plasmas **17**, 032114 (2010).
- ¹⁰A. Spitkovsky, "Simulations of relativistic collisionless shocks: shock structure and particle acceleration," AIP Conference Proceedings **801**, 345–350 (2005).
- ¹¹W. Fox, G. Fiksel, A. Bhattacharjee, P.-Y. Chang, K. Germaschewski, S. X. Hu, and P. M. Nilson, "Filamentation instability of counterstreaming laser-driven plasmas," Phys. Rev. Lett. **111**, 225002 (2013).
- ¹²D. D. Ryutov, N. L. Kugland, H.-S. Park, C. Plechaty, B. A. Remington, and J. S. Ross, "Intra-jet shocks in two counterstreaming, weakly collisional plasma jets," Physics of Plasmas **19**, 074501 (2012).
- ¹³J. S. Ross, S. H. Glenzer, P. Amendt, R. Berger, L. Divol, N. L. Kugland, O. L. Landen, C. Plechaty, B. Remington, D. Ryutov, W. Rozmus, D. H. Froula, G. Fiksel, C. Sorce, Y. Kuramitsu, T. Morita, Y. Sakawa, H. Takabe, R. P. Drake, M. Grosskopf, C. Kuranz, G. Gregori, J. Meinecke, C. D. Murphy, M. Koenig, A. Pelka, A. Ravasio, T. Vinci, E. Liang, R. Presura, A. Spitkovsky, F. Miniati, and H.-S. Park, "Characterizing counter-streaming interpenetrating plasmas relevant to astrophysical collisionless shocks," Physics of Plasmas **19**, 056501 (2012).
- ¹⁴H.-S. Park, D. Ryutov, J. Ross, N. Kugland, S. Glenzer, C. Plechaty, S. Pollaine, B. Remington, A. Spitkovsky, L. Gargate, G. Gregori, A. Bell, C. Murphy, Y. Sakawa, Y. Kuramitsu, T. Morita, H. Takabe, D. Froula, G. Fiksel, F. Miniati, M. Koenig, A. Ravasio, A. Pelka, E. Liang, N. Woolsey, C. Kuranz, R. Drake, and M. Grosskopf, "Studying astrophysical collisionless shocks with counterstreaming plasmas from high power lasers," High Energy Density Physics **8**, 38 – 45 (2012).
- ¹⁵B. A. Trubnikov, "Particle interactions in a fully ionized plasma," Reviews of Plasma Physics **1**, 105 (1965).
- ¹⁶A. A. Vedenov and D. D. Ryutov, "Quasilinear effects in two-stream instabilities," Reviews of Plasma Physics **6**, 1 (1975).
- ¹⁷T. N. Kato and H. Takabe, "Nonrelativistic collisionless shocks in unmagnetized electron-ion plasmas," The Astrophysical Journal Letters **681**, L93–L96 (2008).
- ¹⁸T. R. Boehly, R. S. Craxton, T. H. Hinterman, J. H. Kelly, T. J. Kessler, S. A. Kumpan, S. A. Letzring, R. L. McCrory, S. F. B. Morse, W. Seka, S. Skupsky, J. M. Soures, and C. P. Verdon,

- “The upgrade to the omega laser system,” *Review of Scientific Instruments* **66**, 508–510 (1995).
- ¹⁹J. S. Ross, H.-S. Park, R. Berger, L. Divol, N. L. Kugland, W. Rozmus, D. Ryutov, and S. H. Glenzer, “Collisionless coupling of ion and electron temperatures in counterstreaming plasma flows,” *Phys. Rev. Lett.* **110**, 145005 (2013).
- ²⁰S. C. Wilks, A. B. Langdon, T. E. Cowan, M. Roth, M. Singh, S. Hatchett, M. H. Key, D. Pennington, A. MacKinnon, and R. A. Snavely, “Energetic proton generation in ultra-intense laser–solid interactions,” *Physics of Plasmas* (1994-present) **8**, 542–549 (2001).
- ²¹C. K. Li, F. H. Séguin, J. A. Frenje, J. R. Rygg, R. D. Petrasso, R. P. J. Town, P. A. Amendt, S. P. Hatchett, O. L. Landen, A. J. Mackinnon, P. K. Patel, V. A. Smalyuk, J. P. Knauer, T. C. Sangster, and C. Stoeckl, “Monoenergetic proton backlighter for measuring e and b fields and for radiographing implosions and high-energy density plasmas (invited),” *Review of Scientific Instruments* **77**, 10E725 (2006).
- ²²F. H. Seguin, J. A. Frenje, C. K. Li, D. G. Hicks, S. Kurebayashi, J. R. Rygg, B.-E. Schwartz, R. D. Petrasso, S. Roberts, J. M. Soures, D. D. Meyerhofer, T. C. Sangster, J. P. Knauer, C. Sorce, V. Y. Glebov, C. Stoeckl, T. W. Phillips, R. J. Leeper, K. Fletcher, and S. Padalino, “Spectrometry of charged particles from inertial-confinement-fusion plasmas,” *Review of Scientific Instruments* **74**, 975–995 (2003).
- ²³N. L. Kugland, D. D. Ryutov, C. Plechaty, J. S. Ross, and H.-S. Park, “Invited article: Relation between electric and magnetic field structures and their proton-beam images,” *Review of Scientific Instruments* **83**, 101301 (2012).
- ²⁴This is probability distribution function of the generalized extreme value distribution.
- ²⁵R. Fonseca, L. Silva, F. Tsung, V. Decyk, W. Lu, C. Ren, W. Mori, S. Deng, S. Lee, T. Katsouleas, and J. Adam, “Osiris: A three-dimensional, fully relativistic particle in cell code for modeling plasma based accelerators,” in *Computational Science, ICCS 2002*, Lecture Notes in Computer Science, Vol. 2331, edited by P. Sloot, A. Hoekstra, C. Tan, and J. Dongarra (Springer Berlin / Heidelberg, 2002) pp. 342–351.
- ²⁶M. V. Medvedev and A. Loeb, “Generation of magnetic fields in the relativistic shock of gamma-ray burst sources,” *The Astrophysical Journal* **526**, 697–706 (1999).
- ²⁷R. C. Davidson, D. A. Hammer, I. Haber, and C. E. Wagner, “Nonlinear development of electromagnetic instabilities in anisotropic plasmas,” *Physics of Fluids* **15**, 317–333 (1972).
- ²⁸D. D. Ryutov, F. Fiuza, C. M. Huntington, J. S. Ross, and H.-S. Park, “Collisional effects in the ion weibel instability for two counter-propagating plasma streams,” *Physics of Plasmas* **21**, 032701 (2014).
- ²⁹L. Biermann, “Über den ursprung der magnetfelder auf sternern und im interstellaren raum,” *Zeitschrift für Naturforschung* **5**, 65–71 (1950).
- ³⁰N. L. Kugland, D. D. Ryutov, P.-Y. Chang, R. P. Drake, G. Fiksel, D. H. Froula, S. H. Glenzer, G. Gregori, M. Grosskopf, M. Koenig, Y. Kuramitsu, C. Kuranz, M. C. Levy, E. Liang, J. Meinecke, F. Miniati, T. Morita, a. Pelka, C. Plechaty, R. Presura, a. Ravasio, B. a. Remington, B. Reville, J. S. Ross, Y. Sakawa, a. Spitkovsky, H. Takabe, and H.-S. Park, “Self-organized electromagnetic field structures in laser-produced counter-streaming plasmas,” *Nature Physics* **8**, 809–812 (2012).
- ³¹D. D. Ryutov, N. L. Kugland, M. C. Levy, C. Plechaty, J. S. Ross, and H. S. Park, “Magnetic field advection in two interpenetrating plasma streams,” *Physics of Plasmas* **20**, 032703 (2013).
- ³²N. L. Kugland, J. S. Ross, P.-Y. Chang, R. P. Drake, G. Fiksel, D. H. Froula, S. H. Glenzer, G. Gregori, M. Grosskopf, C. Huntington, M. Koenig, Y. Kuramitsu, C. Kuranz, M. C. Levy, E. Liang, D. Martinez, J. Meinecke, F. Miniati, T. Morita, A. Pelka, C. Plechaty, R. Presura, A. Ravasio, B. A. Remington, B. Reville, D. D. Ryutov, Y. Sakawa, A. Spitkovsky, H. Takabe, and H.-S. Park, “Visualizing electromagnetic fields in laser-produced counter-streaming plasma experiments for collisionless shock laboratory astrophysics,” *Physics of Plasmas* **20**, 056313 (2013).